Stress–strain partitioning behavior and mechanical properties of dual-phase steel using finite element analysis

Ryotaro Maeda, Zhi-Lei Wang*, Toshio Ogawa, Yoshitaka Adachi

Department of materials science and engineering, Nagoya University, Furo-cho, Chikusa-ku, Nagoya 464-8601, Japan

*Corresponding author.

E-mail: wang.zhilei@material.nagoya-u.ac.jp

Tel.: +81 52 789 3577

Abstract

Various industrial applications require materials with both high strength and good ductility. However, strategies for enhancing material performance are usually trapped in a strength–ductility trade-off. In this study, the effect of martensite morphologies (including geometry, connectivity, and distribution direction) on the stress–strain partitioning behavior and mechanical properties of a ferrite-martensite dual phase steel was studied using the secant method and finite element analysis. The results demonstrated that the combination of rhombus and horizontal geometries provided a good balance of

strength and ductility. Thus, a combination of 45° and 0° regarding the angle between the directions of martensite distribution and deformation was further determined to be beneficial to the strength–ductility balance. These results are expected to provide a general understanding of strengthening and toughening mechanisms and will promote the development of high-performance steels.

Keywords: martensite morphology, dual phase steel, strength–ductility balance, secant method, finite element analysis

1. Introduction

Energy shortage and environmental pollution are causing a dramatic escalation of social issues owing to increased industrial combustion of fossil fuels and emissions. The development of ecofriendly materials is an efficient solution to improve sustainable issues for the materials research community. Lightweight and high-strength structural materials (e.g., aluminum and magnum alloys) are receiving increasing interest both in science and engineering communities owing to their great potential in the production of industrial parts (e.g., automotive and aerospace) along with the added benefits of energy conservation, emissions reduction, and safety improvement.

Broad industrial applications require materials with both high strength and good

ductility as well as an economic cost of related manufacturing. However, unfortunately, the strategies for enhancing material strength often cause loss in ductility, which is well-known as the strength–ductility trade-off. Thus, strength maximization without highly compromising ductility has become an important objective while designing high-performance materials. Extensive efforts have focused on dislocation engineering to circumvent the strength–ductility trade-off by choosing novel alloy compositions or processing routes. These efforts have revealed various strategies or theoretical mechanisms for improving the strength–ductility trade-off such as grain refinement [1, 2], enhanced coherent twin boundaries [3, 4], increased alloying elements [5, 6], introduced fine-sized precipitates [7, 8], and phase transformation [9].

Dual-phase (DP) steels consisting of soft and hard phases can alleviate the strength–ductility trade-off owing to their potential strength, good ductility, and economic cost. Studies have demonstrated that the good ductility of DP steels is attributed to the strain hardening behavior of the soft phase through pronounced dislocation activities [10], strain partitioning [11], or strain-induced phase transformation [12]. Good strength originates from interfacial hardening by resisting the dislocation slip within the soft phase by the hard phase [13]; the larger differences in hardness between the hard and soft phases will aggravate the strength–ductility trade-off owing to inevitable microcracks at the interface

[14, 15]. In addition, grain refinement [16, 17] and introduction of chain-networked martensitic islands [18, 19] have also been demonstrated to be beneficial to the strength-ductility balance of DP steels via enhanced of work hardening behavior.

The current strategies to improve the strength–ductility trade-off involve choosing adequate alloy compositions or processing routes followed by mechanism interpretation with a nanoscale dislocation theory. Although such experiment-based strategies have led to considerable achievements in science and engineering, they are often implemented in a case-by-case manner; thus, there is a lack of general and widespread understanding for developing high-performance steels.

Several early theoretical methods, including micromechanics [20], Eshelby's equivalence inclusion principle [21], and Mori–Tanaka mean-field theory [22], have pioneered a common sense in terms of deformation behaviors of multiphase steels. On the basis of previous theories, the secant method has been developed to account for the true stress–strain (σ–ε) partitioning behavior of a DP system [23]. Using the secant method, it has been revealed that the flow stress curve of martensite–ferrite DP steel reaches an upper bound when the matrix is martensite, while it becomes the lower bound when the matrix is ferrite [24]. However, when the configurations of matrix and inclusion are indistinguishable, the σ–ε relation has not yet been well understood. Moreover, the

secant-method-based calculations often assume the shape of the inclusion phase to be a sphere; however, there is no definition regarding the matrix structure.

On the other hand, as data-driven materials research is attracting increasing attention in the materials community to accelerate advances in materials discovery, a machine-learning-based property-to-microstructure inverse analysis approach has been proposed for the design of high-performance steels in our previous work [25]. It was found that a large data volume is critical for an adequate inverse analysis model. However, experiment-based material research is quite inefficient in generating the required data. Thereby, finite element analysis, which is a well-known robust strategy to simulate the complex elastoplastic deformation process concurrent with generating numerous microstructure and property data in an efficient manner, has been employed to study the deformation behaviors of DP microstructures in this study. The effect of martensite morphologies (including its geometry, connectivity, and distribution direction) on the σ–ε partitioning behavior and mechanical properties (tensile strength (TS) and uniform elongation (uEL)) were systematically investigated. This work aims to provide a general perspective in understanding the strengthening and toughening mechanism of steel materials as well as accumulating data for the subsequent data-driven design of high-performance steels.

2. Analysis methods

2.1. Finite element analysis

Two-dimensional (2D) rectangular microstructural patterns (200 × 150 mm) containing 20% of a martensite phase with four geometries (square, triangle, hexagon, and rhombus) and six connectivities (from connected to dispersed) for each geometry (24 patterns in total) were analyzed. Notably, 2D simulation often gives rise to some criticism because real materials are three dimensional (3D). As reported, the flow curves of DP steels are readily underestimated by using 2D plane strain modeling in comparison to those obtained by 3D modeling or experimentation [26, 27]. Nevertheless, it has been found that a lower content of martensite phase of ≤20% could circumvent such underestimation [27]. Thus, static stress analysis was carried out under a 2D plane-large-strain condition to simulate tensile testing in the present work with Femtet commercial software (Murata Software, Co., Ltd., Japan). Triangle element and adaptive mesh refinement with a maximum mesh size of 2 mm were used in the present analysis. The boundary conditions are as follows: in Figure 1, the left short side of the rectangular pattern was constrained and the long sides were free. Tensile loading was applied along the long side direction. Finite element analysis used the true σ and ε data of single-phase

martensite and ferrite as inputs and output of the σ–ε data of the analyzed patterns.

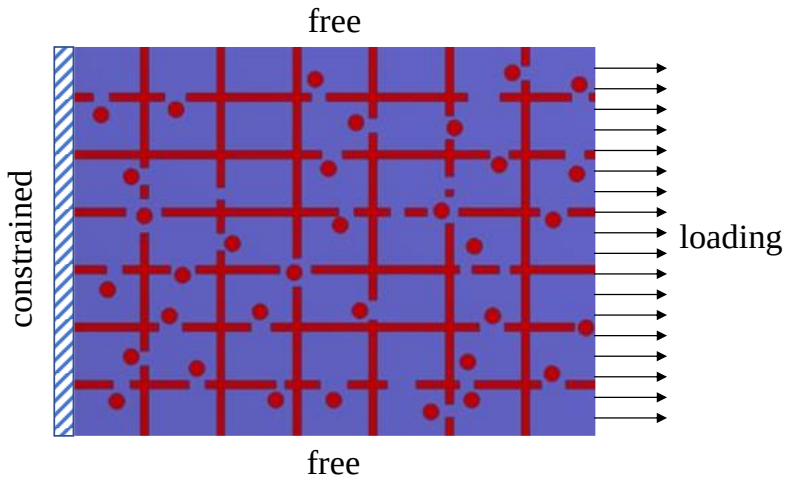

Figure 1. Schematic drawing demonstrating the loading and boundary conditions of the finite element simulation. The red and purple regions represent martensite and ferrite phases, respectively.

2.2. Swift equation

In this study, the σ of single-phase ferrite and martensite was determined by the Swift equation as follows, which is a theoretical empirical formula obtained from true stress and strain [28]:

$$\sigma = a\,(b + \varepsilon)^N \tag{1}$$

where a, b, and N are the constants that depend on chemical compositions and microstructural parameters. The a, b, and N of the ferrite phase were estimated by the following experimental regression formulas [28]:

$$a = 7.19 \times 10^3 C + 133Si + 2.1 \times 10^3 P - 1.01 \times 10^3 Nb + 230d^{-1/2} + 459 \quad (2)$$

$$b = 0.002 \quad (3)$$

$$N = 20.0C + 3.05 \times 10^{-3} Si + 1.24P - 2.54Nb - 0.934d^{-1/2} + 0.299 \quad (4)$$

where d is the ferrite grain size. The a, b, and N values of the martensite phase were estimated as follows:

$$a = 1.06 \times 10^3 C + 1.24 \times 10^2 Mn + 1.0Ni - 0.07d_{(\gamma)} - 34.9I_t + 1.10 \times 10^3 \quad (5)$$

$$b = 10^{-7} \quad (6)$$

$$N = 0.04C + 0.02Mn + 1.2 \times 10^{-3} Ni - 1.7 \times 10^{-5} d_{(\gamma)} - 1.2 \times 10^{-4} I_t + 0.0181 \quad (7)$$

where $d_{(\gamma)}$ and I_t are the prior austenite grain size and temperature parameter, respectively. The details of the adopted chemical composition and microstructural parameters of ferrite and martensite phases and resultant a, b, and N are shown in Table 1.

Table 1. Chemical composition and microstructural parameters of single-phase ferrite and martensite used for the Swift calculation and their a, b, and N.

	C	Mn	Si	P	Ni	Nb	d (μm)	$d_{(\gamma)}$ (μm)	I_t	a	b	N
Ferrite	0.001	-	0.5	0.03	-	0	22	-	-	644	0.002	0.16
Martensite	0.07	2	-	-	2.94	-	-	50	1	1387	10^{-7}	0.06

The mechanical properties of TS and uEL of the analyzed patterns were determined by the following equations, in which a, b, and N for each pattern were estimated through the regression analysis of their σ–ε data using a solver installed in Excel.

$$TS = a\, N^N \tag{8}$$

$$uEL = exp\,(N - b) - 1 \tag{9}$$

2.3. Secant method

When a DP system is subjected to a monotonically increasing proportional loading, the deformation process typically experiences three stages. The first stage is elastic, under which the σ–ε curve is interpreted by its effective elastic modulus. With an increase in stress, the second stage begins when either the inclusion or the matrix enters the plastic range, which leaves the other one in the elastic state. A continuous increase of applied stress will eventually cause the elastic phase to yield, which brings the system to DP plasticity, i.e., the third stage.

The σ–ε partitioning behavior of a DP system under stages 2 and 3 with the secant method is illustrated in Figure 2(a). In this figure, the matrix (phase 0) has an imaginary secant modulus (L_0^s) under $\varepsilon^{(0)}$ and $\sigma^{(0)}$, and the inclusion (phase 1) is subjected to plastic strain ($\varepsilon^{p(1)}$) with $\varepsilon^{(1)}$ and $\sigma^{(1)}$. Thus, the partitioned σ and ε of the DP system (phase 0+1) with an inclusion volume fraction of $\frac{\sigma^{(1)}-\sigma^{(0)}}{\bar{\sigma}-\sigma^{(0)}}$ can be represented by $\bar{\sigma}$ and $\bar{\varepsilon}$, respectively. Figure 2(b) shows the σ–ε curves of single-phase ferrite and martensite and the calculated upper and lower bounds of the σ–ε curve for a DP system with the

martensite volume fraction of 0.2. The partitioning behaviors for upper and lower bounds are plotted until their TS points.

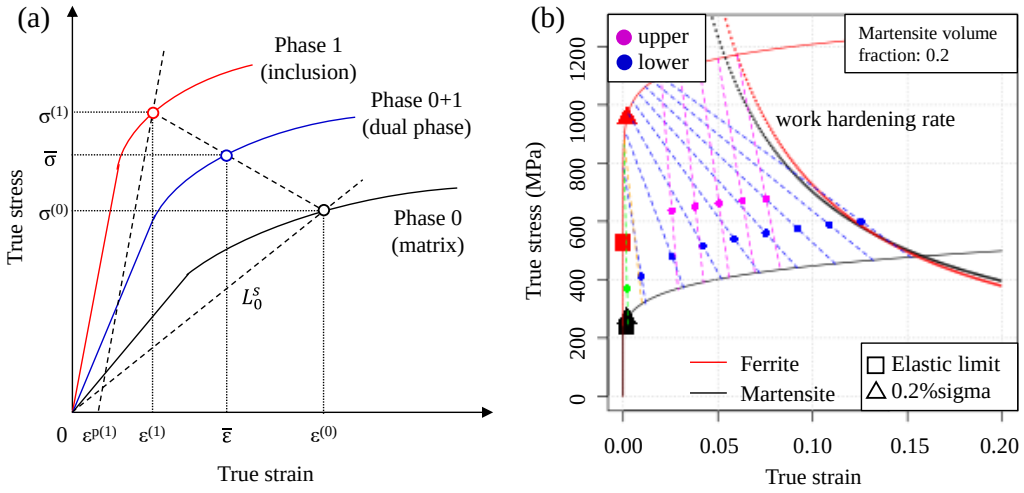

Figure 2. (a) Schematic illustration of the secant method. (b) σ–ε curves of single-phase ferrite and martensite and the upper and lower bounds of a DP system with the martensite volume fraction of 0.2.

3. Results and discussion

The σ–ε curves of the analyzed patterns in an elastoplastic stage are shown in Figure 3. Of note, the early ductile fracture of martensite is not considered in this study. Different partitioning behaviors of σ and ε were clearly observed with changes in connectivity of martensite. The P1 (chain-networked martensite) and P6 (dispersed martensite) patterns refer to the upper and lower bonds, respectively, which suggests that chain-networked martensite in P1 can be identified as the matrix, and dispersed martensite in P6 is the

inclusion. When the matrix configuration is percolated, i.e., medium connectivity degree of martensite (P2, P3, P4, and P5), the σ–ε curve is located between those two bounds. With a decrease in the connectivity degree from P1 to P6, the σ–ε curve tended toward the lower bound. However, such tendency gradually became unnoticeable with a change in the martensite geometry from square to triangle to hexagon to rhombus. According to the secant method calculation result (Figure 2(b)), the upper and lower bounds can be assumed to be constant. On the basis of this assumption, it was inferred that martensite geometry also strongly correlates with the σ–ε partitioning behaviors and mechanical properties.

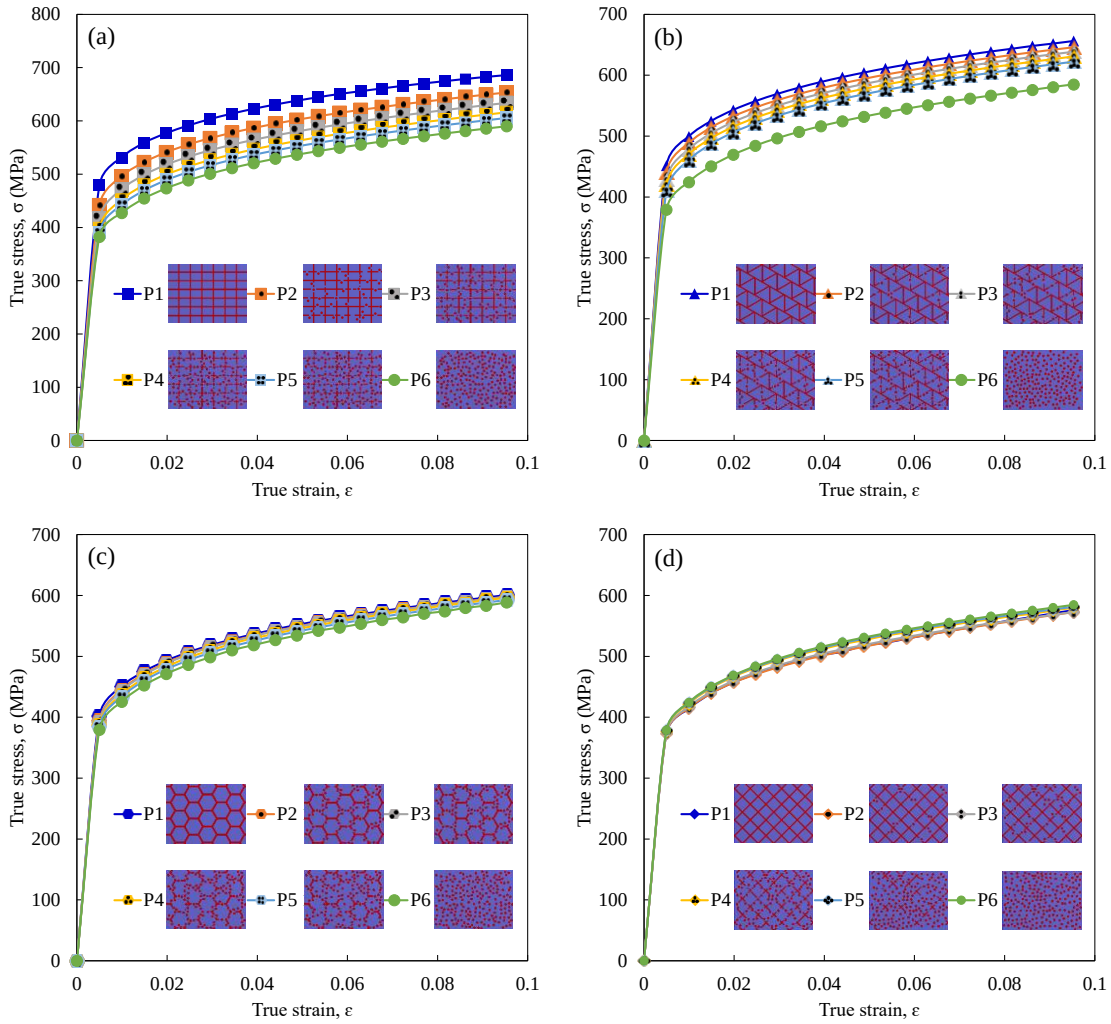

Figure 3. σ–ε curves of the analyzed patterns with martensite geometries of (a) square, (b) triangle, (c) hexagon, and (d) rhombus.

The estimated TS and uEL of the studied patterns are shown in Figure 4. With a decrease in the connectivity degree of martensite from P1 to P6, the square and triangle patterns exhibited a considerable strength–ductility trade-off, in which TS and uEL were noticeably decreased and increased, respectively. However, the strength–ductility trade-off was no longer evident for the hexagon geometry, and even a contrary result was

observed for the rhombus geometry. Considering the assumption of constant upper and lower bounds for the σ–ε curve (i.e., deviations in TS and uEL caused by martensite connectivity are consistent), the weakened strength–ductility trade-off can be reasonably attributed to compensation by the geometry factor. The TS of upper and lower bounds calculated by the secant method was estimated to be 673 MPa and 600 MPa, respectively, (ΔTS = 73 MPa). The upper and lower bounds of TS for the square geometry were calculated to be 699 MPa (P1) and 622 MPa (P6), respectively (ΔTS = 77 MPa). However, the other geometries exhibited much lower TS levels compared with that calculated by the secant method. This result implies that square geometry readily intensifies strength, and other geometries, especially the rhombus geometry, decrease strength.

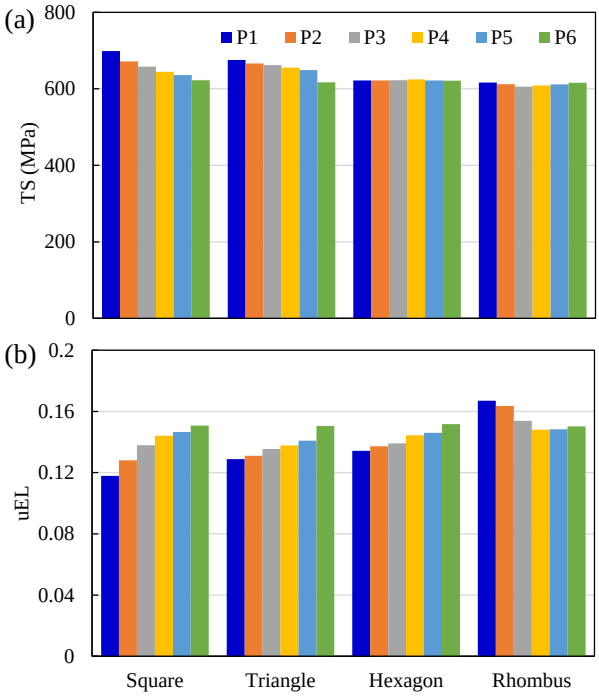

Figure 4. Mechanical properties of (a) TS and (B) uEL of the studied patterns.

Von Mises stress and strain, which are widely used indicators for interpreting stress and strain distributions during plastic deformation [29-31], were employed to investigate the relationship between microstructural configuration and mechanical properties. As local stress concentration is always concurrent with local strain concentration, stress distribution was used to interpret the stress-strain behaviors. Figure 5 shows the von Mises stress maps of the patterns at $\varepsilon = 0.05$. As illustrated in the square patterns (left column), stress concentration is located at the martensite phase. With a decrease in the connectivity degree of martensite, stress concentration is gradually released. With the change in geometry from square to triangle to hexagon to rhombus, the stress concentration becomes weak. As mentioned earlier, the good strength of DP steels originates from a hardening manner caused by the hard phase [13]. Thus, higher TS may be associated with severe stress concentration at the martensite phase.

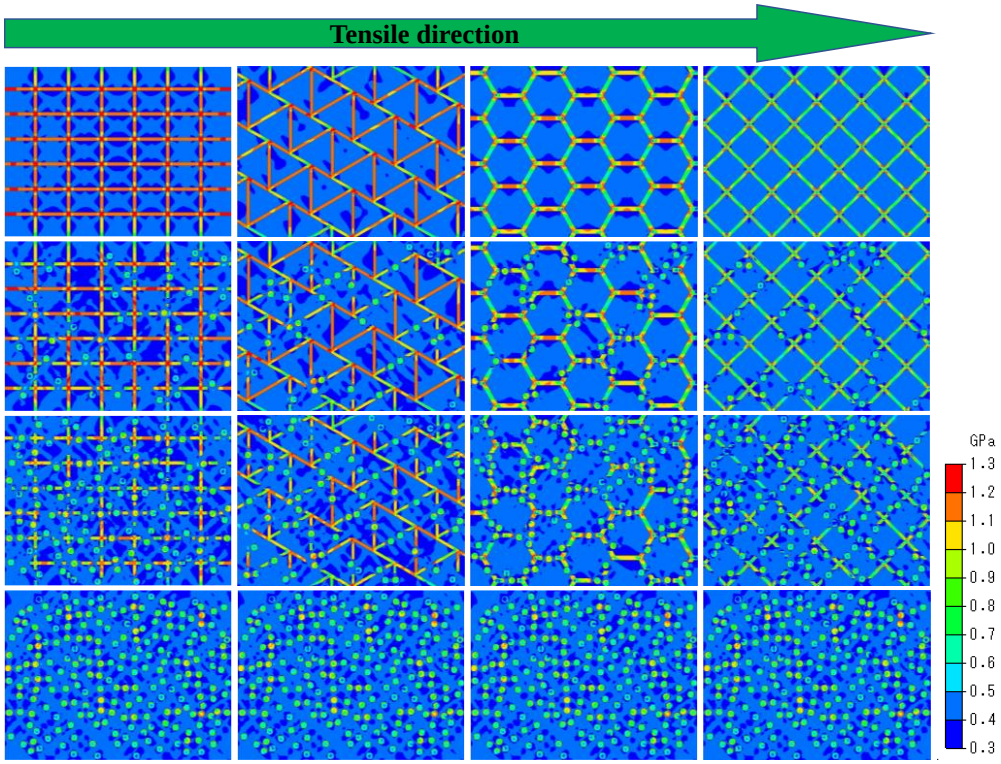

Figure 5. Von Mises stress maps of the studied patterns at $\varepsilon = 0.05$.

It is worth mentioning that horizontal and vertical martensite regions readily induce stress concentration, as shown in the square, triangular, and hexagonal patterns, while a 45° distribution appears to circumvent stress concentration, as indicated in the rhombus pattern. This result suggests a strong correlation between stress concentration and the distribution direction of martensite. Furthermore, some regions of the ferrite phase in the vicinity of stress-concentrated martensite exhibit lower von Mises stress (navy blue regions), which may imply that such stress-concentrated martensite regions act as an obstacle to restrict deformation progression.

The von Mises stress distributions of the studied patterns at σ = 550 MPa are shown in Figure 6. With the martensite geometry changing from square to triangle to hexagon to rhombus, the von Mises stress of the ferrite phase considerably increases. Likewise, with a decrease in the connectivity degree of martensite, the von Mises stress of ferrite for the square, triangle, and hexagon patterns increases, while it appears to decrease for the rhombus patterns. Therefore, assuming that good ductility of DP steels results from a strain hardening behavior of the soft phase [10], the higher uEL of rhombus patterns is likely to be associated with a higher stress in the ferrite phase.

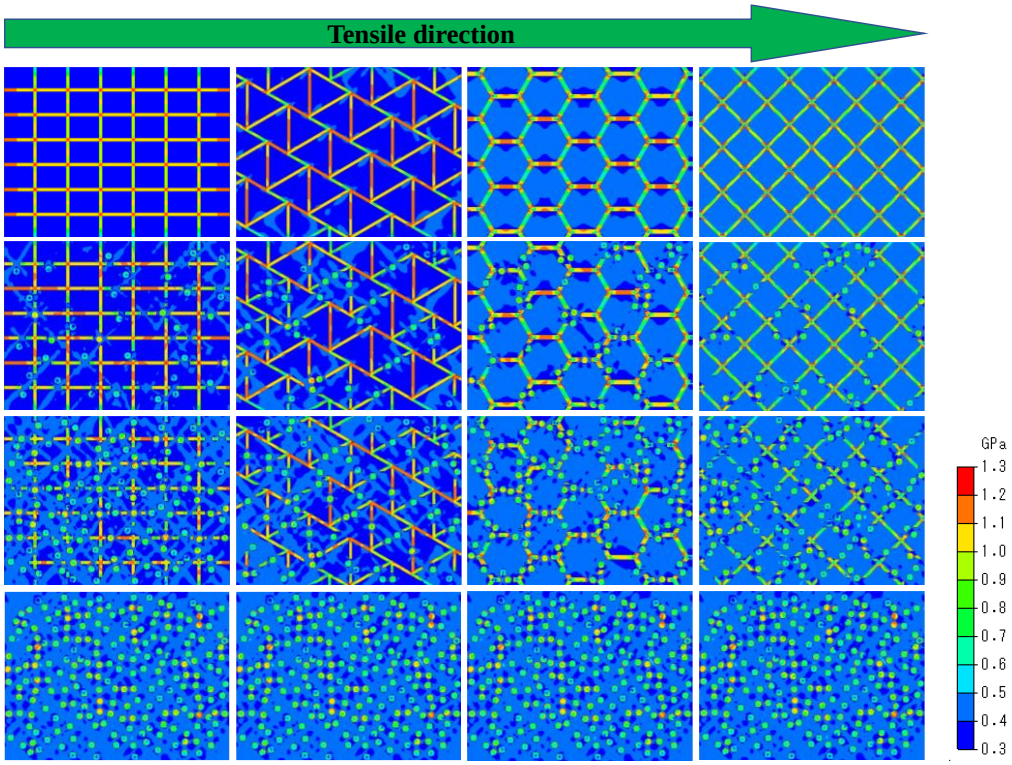

Figure 6. Von Mises stress maps of the studied patterns at σ = 550 MPa.

It is interesting that the P1 pattern of rhombus geometry strongly circumvents the strength–ductility trade-off. At ε = 0.05, the differences between average von Mises stresses of martensite and ferrite for the square, triangle, hexagon, and rhombus P1 patterns were estimated to be 731, 676, 523, and 455 MPa, respectively. It is known that a larger strength difference between hard and soft phases easily causes inevitable microcracks at their interface during deformation, which results in bad ductility [14, 15]. Thus, such a circumventing manner of strength–ductility trade-off for the rhombus P1 pattern is probably due to the smaller stress gradient between martensite and ferrite.

As shown in Figure 4, a square geometry readily enhances strength, while rhombus geometry enhances ductility. Thus, the pattern of martensite with rhombus and horizontal geometry was further evaluated in this study. Figure 7(a) shows its σ–ε curve and estimated TS and uEL. As expected, the combined pattern provides a satisfactory uEL (0.14) and enhanced TS (659 MPa) compared with the rhombus pattern. As shown in Figure 7(b), its von Mises stress analysis at ε = 0.05 demonstrates that the better balance of strength and ductility is attributed to stress concentration located at horizontal martensite; most of ferrite regions remain a uniform von Mises stress except for some low stress regions in the vicinity of geometric intersections; the difference of average von Mises stress between martensite and ferrite showed a medium value of 543 MPa.

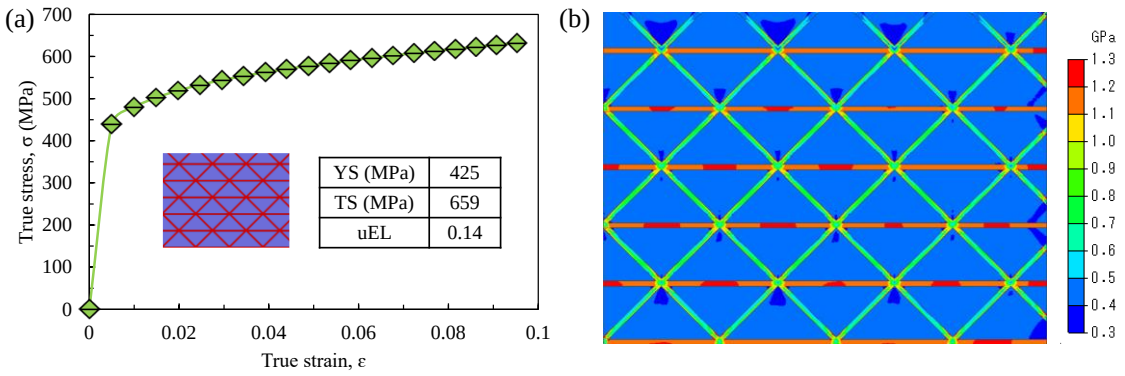

Figure 7. (a) σ–ε curve and mechanical properties of a pattern with martensite geometry (rhombus and horizontal) and (b) its von Mises stress map at $\varepsilon = 0.05$.

A comparison of the balance of TS and uEL for the overall studied patterns expressed by their product (TS×uEL) is shown in Figure 8, where two patterns with horizontal and vertical martensite are also included as a reference. With a decrease in the connectivity degree of martensite, the TS×uEL of square, triangular, and hexagonal patterns is increased; however, TS is considerably compromised. The rhombus pattern with chain-networked martensite provides the largest TS×uEL, while its TS is criticized. With regard to the combined pattern, although its TS×uEL is not considerably improved, it provides a good balance of TS and uEL.

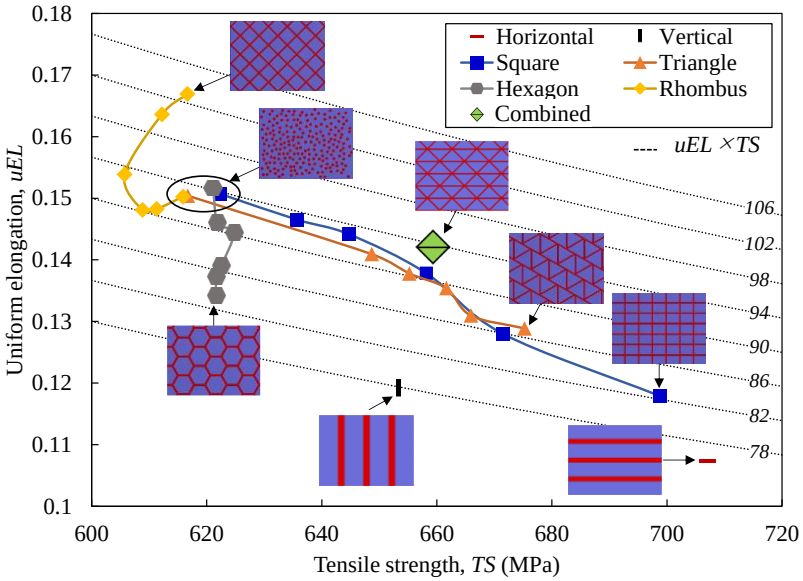

Figure 8. Uniform elongation against tensile strength for the studied patterns.

As mentioned above, the mechanical properties exhibit a correlation with martensite distribution direction, where the angles of 0° and 90° with the deformation direction readily increase strength, and 45° tends to enhance ductility, as identified in square and rhombus patterns. Figure 9 shows a three-dimensional map that demonstrates the relationship between the mechanical properties and martensite distribution angle, which is based on the studied patterns. The x, y, and z-axes of the three-dimensional space represent the fractions of 90, 0, and 45°, respectively. The table shown in Figure 9 provides the proportions of martensite within the evaluated patterns regarding the three angles. The map clearly shows that the high fractions of 90° and 0° correspond to higher strength and lower ductility (illustrated by square, horizontal, and vertical patterns in the

yellow region); the medium fractions of 90° and 0° are related to lower strength and ductility (illustrated by a hexagon pattern in the green region); the high fractions of 45° tend to have higher ductility and lower strength (illustrated by a rhombus pattern in the red region); the medium fractions of 0° and 45° are beneficial to balanced properties of strength and ductility (illustrated by a complexed pattern in the blue region). In addition, the dispersed pattern is assigned to be the origin coordinate without the fractions of 90, 0, and 45°, which suggests that the lower connectivity degree is pointing toward lower strength and medium ductility (purple region).

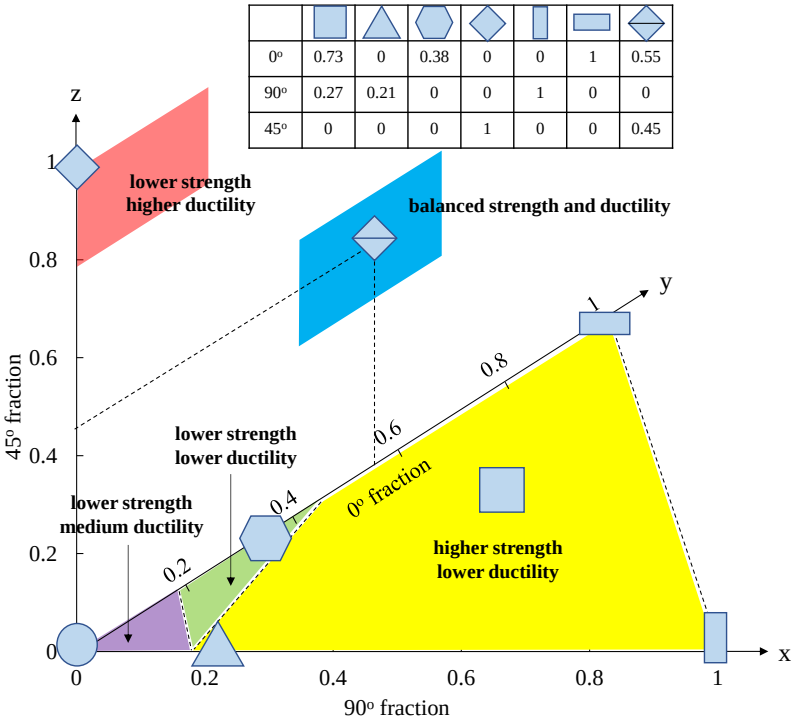

Figure 9. Three-dimensional map demonstrating the dependence of mechanical properties on the angles between the directions of martensite distribution and deformation based on the studied patterns.

The effect of martensite morphologies on σ–ε partitioning behaviors and mechanical properties of DP steel have been systematically investigated in this study. It should be pointed out that, although the DP microstructures involved in this study cannot be reproduced experimentally to real microstructures, a real microstructure can present ideal features locally. Thus, the results are believed to be helpful for a general understanding of the strengthening and toughening mechanisms of multiphase steels. Furthermore, based on the angle relation between the directions of martensite distribution and deformation, to some extent the shortage in strength or ductility could be further circumvented through choosing clever shaping and processing strategies. Therefore, the findings in terms of the angle relationship of mechanical properties may allow one to create a protocol to further improve the material performance for a given industrial application for which intelligent choices of product processing and shaping strategies can be developed.

4. Summary

In this study, the influence of martensite morphologies (including geometry, connectivity, and distribution direction) on the σ–ε partitioning behaviors and mechanical properties of a ferrite-martensite DP steel was studied with the secant method and finite

element analysis. The microstructures with chain-networked martensite and dispersed martensite provided the upper and lower bounds of the σ–ε curve. Square geometry improved the strength owing to the higher stress concentration of martensite, while the rhombus geometry readily enhanced ductility owing to the smaller stress gradient between martensite and ferrite. A combination of rhombus and horizontal geometries provided a good balance of strength and ductility. The angles of 90° and 0° between martensite distribution direction and deformation direction were determined to be beneficial to strength; the 45° angle readily promoted ductility; and the combination of 45° and 0° angles resulted in a good balance of strength and ductility.

Acknowledgements

The research did not receive any specific grant from funding agencies in the public, commercial, or not-for-profit sectors.

References

[1] Y. Wang, M. Chen, F. Zhou, E. Ma, High tensile ductility in a nanostructured metal, Nature 419 (2002) 912–915.

[2] X. Wu, M. Yang, F. Yuan, G. Wu, Y. Wei, X. Huang, Y. Zhu, Heterogeneous lamella structure unites ultrafine-grain strength with coarse-grain ductility, Proc. Natl. Acad. Sci. 112 (2015) 14501–14505.

[3] L. Lu, Y. Shen, X. Chen, L. Qian, K. Lu, Ultrahigh strength and high electrical conductivity in copper, Science 304 (2004) 422–426.

[4] K. Lu, L. Lu, S. Suresh, Strengthening materials by engineering coherent internal boundaries at the nanoscale, Science 324 (2009) 349–352.

[5] S.W. Lee, K.Y. Lee, B.C. De Cooman, Ultra fine-grained 6wt.% manganese TRIP steel, Trans Tech Publications, 2010.

[6] J. Shi, X.J. Sun, M.Q. Wang, W.J. Hui, H. Dong, W.Q. Cao, Enhanced work-hardening behavior and mechanical properties in ultrafine-grained steels with large-fractioned metastable austenite, Scripta Mater. 63 (2010) 815–818.

[7] X.D. Wang, B.X. Huang, L. Wang, Y.H. Rong, Microstructure and mechanical properties of microalloyed high-strength transformation-induced plasticity steels, Metall. Mater. Trans. A 39 (2008) 1–7.

[8] E.V. Pereloma, I.B. Timokhina, K.F. Russell, M.K. Miller, Characterization of clusters and ultrafine precipitates in Nb-containing C–Mn–Si steels, Scripta Mater. 54 (2006) 471–476.

[9] Z.J. Xie, G. Han, W.H. Zhou, X.L. Wang, C.J. Shang, R.D.K. Misra,. A novel multi-step intercritical heat treatment induces multi-phase microstructure with ultra-low yield ratio and high ductility in advanced high-strength steel, Scripta Mater. 155 (2018) 164–168.

[10] J. Kadkhodapour, S. Schmauder, D. Raabe, S. Ziaei-Rad, U. Weber, M. Calcagnotto, Experimental and numerical study on geometrically necessary dislocations and non-homogeneous mechanical properties of the ferrite phase in dual phase steels, Acta Mater. 59 (2011) 4387–4394.

[11] B.L. Ennis, E. Jimenez-Melero, E.H. Atzema, M. Krugla, M.A. Azeem, D. Rowley, D. Daisenberger, D.N. Hanlon, P.D. Lee, Metastable austenite driven work-hardening behaviour in a TRIP-assisted dual phase steel, Int. J. Plast. 88 (2017) 126–139.

[12] M.M. Wang, C.C. Tasan, D. Ponge, A.C. Dippel, D. Raabe, Nanolaminate transformation-induced plasticity-twinning-induced plasticity steel with dynamic strain partitioning and enhanced damage resistance, Acta Mater. 85 (2015) 216–228.

[13] H. Ghassemi-Armaki, R. Maaß, S.P. Bhat, S. Sriram, J.R. Greer, K.S. Kumar,

Deformation response of ferrite and martensite in a dual-phase steel, Acta Mater. 62 (2014) 197–211.

[14] N. Fujita, N. Ishikawa, F. Roters, C.C. Tasan, D. Raabe, Experimental–numerical study on strain and stress partitioning in bainitic steels with martensite–austenite constituents, Int. J. Plast. 104 (2018) 39–53.

[15] D.K. Kim, E.Y. Kim, J. Han, W. Woo, S.H. Choi, Effect of microstructural factors on void formation by ferrite/martensite interface decohesion in DP980 steel under uniaxial tension, Int. J. Plast. 94 (2017) 3–23.

[16] M. Calcagnotto, D. Ponge, D. Raabe, Effect of grain refinement of 1 μm on strength and toughness of dual-phase steels, Mater. Sci. Eng. A 527 (2010) 7832–7840.

[17] M. Nouroozi, H. Mirzadeh, M. Zamani, Effect of microstructural refinement and intercritical annealing time on mechanical properties of high-formability dual phase steel, Mater. Sci. Eng. A, 736 (2018) 22–26.

[18] A. Kalhor, M. Soleimani, H. Mirzadeh, V. Uthaisangsuk, A review of recent progress in mechanical and corrosion properties of dual phase steels, Arch. Civ. Mech. Eng. 20 (2020) 1–14.

[19] N. Nakada, Y. Arakawa, K.S. Park, T. Tsuchiyama, S. Takaki, Dual phase structure formed by partial reversion of cold-deformed martensite, Mater. Sci. Eng. A 553 (2012)

128–133.

[20] Y. Tomota, K. Kuroki, T. Mori, I. Tamura, Tensile deformation of two-ductile-phase alloys: Flow curves of α-γFeCrNi alloys, Mater. Sci. Eng. A 24 (1976) 85–94.

[21] J.D. Eshelby, The determination of the elastic field of an ellipsoidal inclusion, and related problems, Proc. R. Soc. A 241 (1957) 376–396.

[22] T. Mori, K. Tanaka, Average stress in matrix and average elastic energy of materials with misfitting inclusions, Acta. Metall. 21 (1973) 571–574.

[23] G.J. Weng, The overall elastoplastic stress–strain relations of dual-phase metals, J. Mech. Phys. Solids 38 (1990) 419–441.

[24] T. Ohnuki, K. Asoo, Y. Tomota, S. Harjo, Stress partitioning behavior of a DP steel studied by in situ neutron diffraction, J. ISIJ 97 (2011) 45–47.

[25] Z.L. Wang, Y. Adachi, Property prediction and properties-to-microstructure inverse analysis of steels by a machine-learning approach, Mater. Sci. Eng. A 744 (2019). 661–670.

[26] C. Thomser, Modelling of the mechanical properties of dual phase steels based on microstructure. Ph.D. Thesis, RWTH-Aachen, Germany, 2009.

[27] A. Ramazani, K. Mukherjee, H. Quade, U. Prahl, W. Bleck, Correlation between 2D and 3D flow curve modelling of DP steels using a microstructure-based RVE approach,

Mater. Sci. Eng. A 560 (2013) 129–139.

[28] N. Tsuchida, S. Harjo, T. Ohnuki, Y. Tomota, Stress–strain curves of steels, J. ISIJ 100 (2014) 1191–1206.

[29] W.D. Nix, Mechanisms and controlling factors in creep fracture, Mater. Sci. Eng. A 103 (1988) 103–110.

[30] A. Pegoretti, L. Fambri, G. Zappini, M. Bianchetti, Finite element analysis of a glass fibre reinforced composite endodontic post, Biomaterials 23 (2002) 2667–2682.

[31] L. Pierrisnard, F. Bohin, P. Renault, M. Barquins, Coronoradicular reconstruction of pulpless teeth: A mechanical study using finite element analysis, J. Prosthet. Dent. 88 (2002) 442–448.